Nickel boride (Ni$_x$B) as a highly efficient catalyst for oxygen evolution

1

2

3 Justus Masa[a*], Ilya Sinev[b], Hemma Mistry[b,c], Edgar Ventosa[a], Maria de la Mata[e], Jordi Arbiol[e,f], Martin

4 Muhler[d], Beatriz Roldan Cuenya[b], Wolfgang Schuhmann[a*]

5

6 [a] Analytical Chemistry - Center for Electrochemical Sciences (CES), Ruhr-Universität Bochum, Universitätsstr.

7 150, D-44780 Bochum (Germany)

8 [b] Department of Physics, Ruhr-Universität Bochum, Universitätsstr. 150, D-44780 Bochum (Germany)

9 [c] Department of Physics, University of Central Florida, Orlando, FL 32816, USA

10 [d] Laboratory of Industrial Chemistry, Ruhr-Universität Bochum, Universitätsstr. 150, D-44780 Bochum (Germany)

11 [e] Catalan Institute of Nanoscience and Nanotechnology (ICN2), CSIC, and The Barcelona Institute of Science and

12 Technology (BIST), Campus UAB, Bellaterra, 08193 Barcelona, Catalonia, Spain

13 f ICREA, Pg. Lluís Companys 23, 08010 Barcelona, Catalonia, Spain

14 * Correspondence should be addressed to: justus.masa@rub.de and wolfgang.schuhmann@rub.de

15

Abstract

17 The overriding obstacle to mass hydrogen production as the premium fuel for powering our

18 planet is the frustratingly slow kinetics of the oxygen evolution reaction (OER). Additionally,

19 inadequate understanding of the key barriers of the OER is a hindrance to insightful design of

20 advanced OER catalysts. Herein, we present amorphous nickel boride (Ni$_x$B) as a low-cost, very

21 efficient and stable catalyst for the OER during electrochemical water splitting. The catalyst

22 afforded 10 mA cm^{-2} at 0.38 V overpotential during OER in 1.0 M KOH, which reduced to only

23 0.28 V at 20 mA cm^{-2} when supported on nickel foam. *Operando* XAFS measurements revealed

24 prevalence of NiOOH, as well as Ni-B under OER conditions, owing to a Ni-B core@nickel

25 oxyhydroxide shell (Ni-B@NiO$_x$H) structure, and increase in disorder of the NiO$_x$H layer, thus

26 unveiling important insight into the transient states of the catalyst during oxygen evolution.

27

28 **Keywords**: Nickel boride, water oxidation, water splitting, hydrogen evolution, oxygen

29 evolution, XAFS

30

31

32   Electrochemical water splitting for hydrogen production is impeded by intensive energy

33   consumption mostly due to the slow kinetics of the oxygen evolution reaction (OER), and the

34   requirement to use costly and rare platinum group metal (PGM) catalysts, rendering the process

35   of low economic appeal[1,2]. Efforts to reduce or completely substitute the use of PGM

36   electrocatalysts (Pt, IrO_2 and RuO_2), the state-of-the catalysts for electrochemical water splitting

37   (ECWS), with less costly alternatives to leverage the competitiveness of ECWS have been futile

38   in the past[1]. Moreover, even with Pt as the cathode, and RuO_2 or IrO_2 as the anode, large

39   overpotentials are still incurred to achieve meaningful electrolysis rates[3,4]. ECWS using non-

40   precious metal catalysts is more promising in high pH electrolytes, where Ni, Co and Fe-based

41   materials are very promising[5,6]. Specifically, mixed metal oxides and hydroxides with a layered

42   structure[7–11], and compounds of Co and Ni incorporating non-metal elements, typically, B, N, S,

43   Se and P, have proved phenomenal in alkaline water oxidation, with activities surpassing RuO_2

44   and IrO_2 being reported for $NiSe^{5}$, $Ni_5P_4{}^{6}$, Ni_2P^{7}, $CoP^{8,12}$, $Ni_3N^{9,10}$, among others. Meanwhile,

45   binary and ternary compounds of Co, Fe, Mo, W, and Ni with B, P, S, and Se, among others, also

46   exhibit outstanding activity in catalyzing the hydrogen evolution reaction (HER)[13–18]. These

47   developments inspire new directions in the search for advanced non-precious catalysts for

48   ECWS.

49   Herein, we show that nickel boride (Ni_xB) is a remarkably active and stable non-precious

50   metal catalyst for oxygen evolution under alkaline conditions. The catalyst afforded 10 mA cm^{-2}

51   at 0.38 V overpotential during OER in 1.0 M KOH, which reduced to only 0.28 V at 20 mA cm^{-2}

52   when supported on nickel foam. Additionally, we present insight from *operando* XAFS of the

53   nature of transient states of the catalyst during oxygen evolution. The active form of the catalyst

54   is a Ni-B@NiOOH (core@shell) structure. We observed a contraction of the Ni-O bonds in

55   NiOOH accompanied with increase in disorder of the layer during active oxygen evolution.

56

Catalyst preparation and characterization

57

58   Nickel boride (Ni_xB) was prepared by chemical reduction of nickel ions in a deaerated 1.0 M

59    $NiCl_2{*}6\ H_2O_{(aq)}$ solution using 1.0 M $NaBH_{4(aq)}$ (see SI for details). The composition of Ni and B

60   in the product was 76.2 % and 6.6 % respectively, corresponding to a Ni:B stoichiometry of 2:1

61   (Table S1), the rest being mostly oxygen (Fig. S1). X-ray diffraction (XRD) studies (Fig. 1)

62   revealed Ni_xB to be XRD amorphous. The product remains XRD amorphous upon annealing

under Ar at 300 ^{o}C for 2 h. Further increase of the annealing temperature to 600°C led to crystallization and emergence of Ni$_3$B (ICSD: 614985) as the major phase, and Ni$_2$B (ICSD 75792) as a minor phase. Ni$_3$B remained the dominant phase in the sample annealed at 1000 ^{o}C, with minor reflections assignable to Ni$_2$B also detectable. Structure refinement using Rietveld analysis revealed that Ni$_x$B-1000 contained 79% Ni$_3$B while Ni$_2$B made up 21%. Ni$_x$B annealed at 300 ^{o}C (Ni$_x$B-300) exhibited the best electrochemical performance (discussed later) and was thus characterized in more detail.
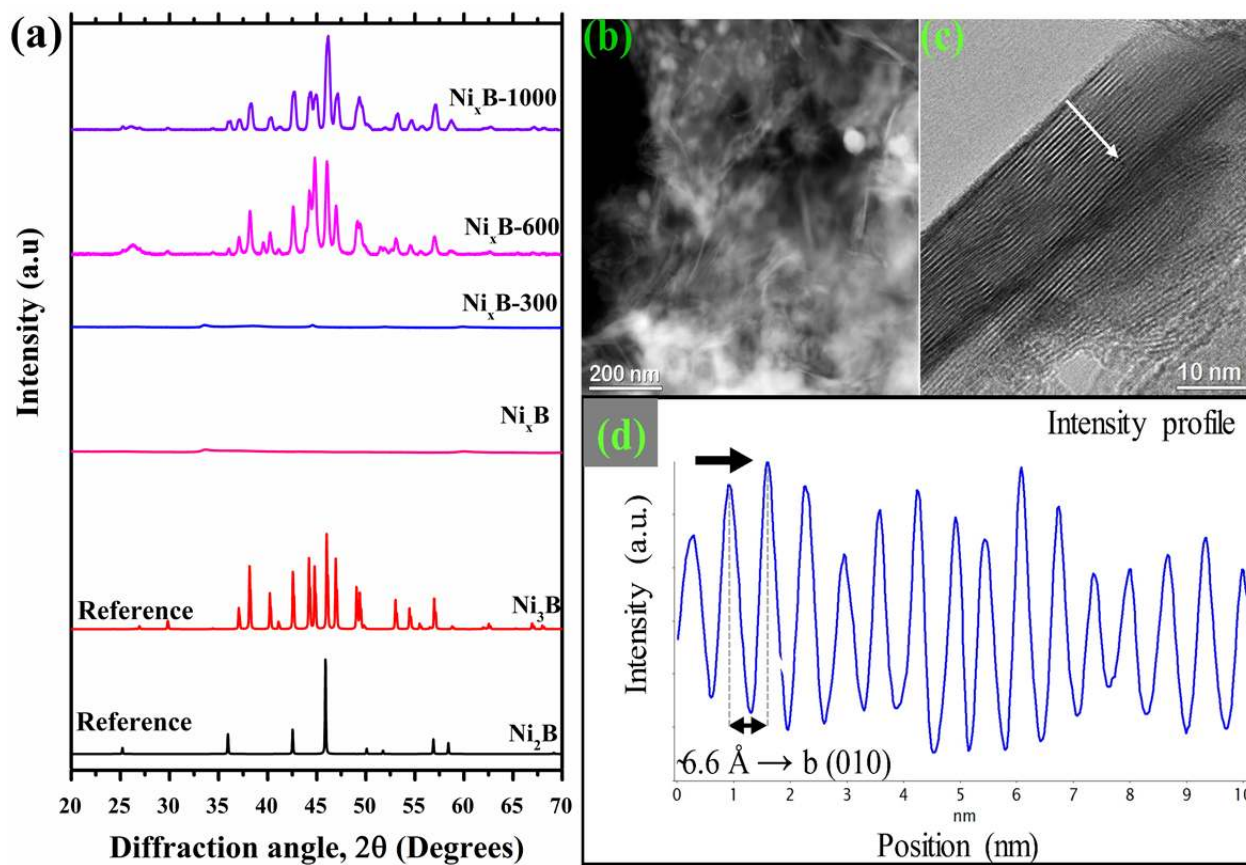
Figure 1| (a) XRD pattern of Ni$_x$B, Ni$_x$B annealed at 300 ^{o}C (Ni$_x$B-300), 600 ^{o}C (Ni$_x$B-600), and at 1000 ^{o}C (Ni$_x$B-1000), and of the references Ni$_2$B (ICSD 75792) and Ni$_3$B (ICSD 614985). (b) High-angle annular dark field (HAADF) low magnification TEM micrograph of Ni$_x$B-300, (c) HRTEM of a single particle showing layers of sheets, (d) intensity profile taken across the flake along the white arrow in (c) showing individual sheets with a thickness of $\approx$ 6.6 Å.

Ni$_x$B-300 comprised of very thin sheets as well as discrete particles (Fig. 1b). High resolution TEM (HRTEM) analysis of an individual flake of Ni$_x$B-300 (Fig. 1c) reveals atomically thin layers with a thickness of about 6.6 Å (Fig. 1d). Spectroscopic analysis by

81　electron energy loss spectroscopy (EELS) shows that the discrete particles are predominantly

82　nickel boride, while the sheets have a uniform distribution of Ni, B, as well as oxygen (Fig. S3).

83　Fast Fourier Transform (FFT) analysis of selected regions of the HRTEM images disclosed

84　predominance of Ni_2B nanocrystallites in Ni_xB-300 (Fig. S4). Crystallites of Ni_3B were also

85　occasionally found (Fig. S5). In consideration of the XRD and TEM observations, it can be

86　concluded that Ni_xB-300 was composed of nanocrystallites of Ni_2B, and Ni_3B to a less extent, as

87　well as very small particles of $Ni^{(0)}$. The predominance of the Ni_3B phase at high annealing

88　temperatures, as confirmed by XRD, indicates thermally induced phase transition of Ni_2B to

89　Ni_3B, and also suggests the reaction of Ni with Ni_2B to form Ni_3B ($Ni + Ni_2B \rightarrow Ni_3B$),

90　consistent with the work by Glavee et al.[19,20] among others.

91　**XPS and XAFS characterization**

92　XPS examination of the chemical state of as prepared Ni_xB minimally exposed to air showed the

93　main Ni $2p_{3/2}$ and Ni $2p_{1/2}$ core peaks at 852.5 eV and 869.6 eV (Fig. 2a(i)), respectively, typical

94　of Ni_2B[21]. The Ni $2p_{3/2}$ and Ni $2p_{1/2}$ satellite peaks at 855.6 eV and 873.0 eV, respectively, are

95　due to Ni^{2+}, indicating the presence of surface oxide or hydroxide species. Amorphous metal

96　borides are spontaneously oxidized when exposed to air and water to form surface

97　oxides/hydroxides leading to a core@shell (metal boride@metal oxide/hydroxide) structure[22–24].

98　Ni_xB exposed to air, (Fig. 2a(ii), thus exhibited a predominantly oxidized surface with a

99　dominant Ni $2p_{3/2}$ peak at 855.82 eV (Ni^{2+} species) and minor peak at 852.52 eV due to the

100　interaction of nickel with boron (Fig. 2a). A positive chemical shift of 0.95 eV in the binding

101　energy of the Ni $2p_{3/2}$ peak was observed upon annealing Ni_xB at 300 ^{o}C (Fig 2c), indicating

102　relative displacement of electrons from nickel. The annealing process thus led to modification of

103　the surface electronic structure of Ni_xB-300, which had a beneficial effect on its OER activity.

104　The B 1s spectrum of as prepared Ni_xB minimally exposed to air (Ni_xB-(i) in Fig 2b) was

105　deconvoluted into two distinct species at 187.9 eV and 191.8 eV (Fig. 2b). The species at 187.9

106　eV is due to interaction of boron with nickel, whereas the one at 191.8 eV is due to boron-oxo

107　species. On the other hand, the B 1s spectrum of Ni_xB exposed to air for several hours (Ni_xB-(ii)

108　in Fig 2b) was deconvoluted into two contributions at 190.07 eV and 192.0 eV both

109　corresponding to boron oxide species. The O 1s spectrum of Ni_xB-300 (Fig 2d), not activated

110　sample, shows that its surface was covered with $Ni(OH)_2$. Meanwhile, after electrochemical

activation (activated in Fig 2d), which involved 50 cycles of potential cycling in 1.0 KOH between 0.95 V and 1.65 V vs RHE, the surface was mainly covered with a nickel oxyhydroxide (NiOOH) layer.
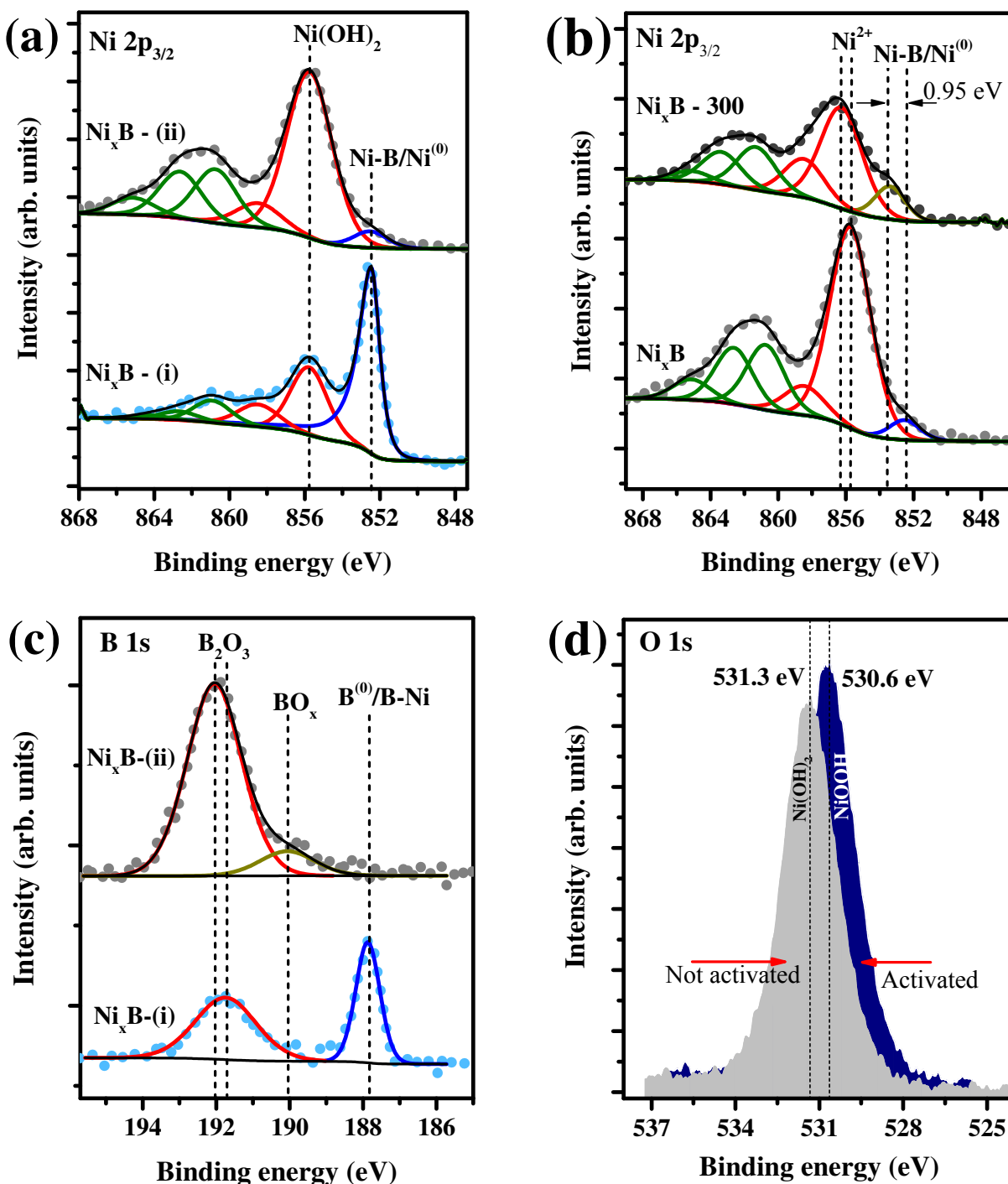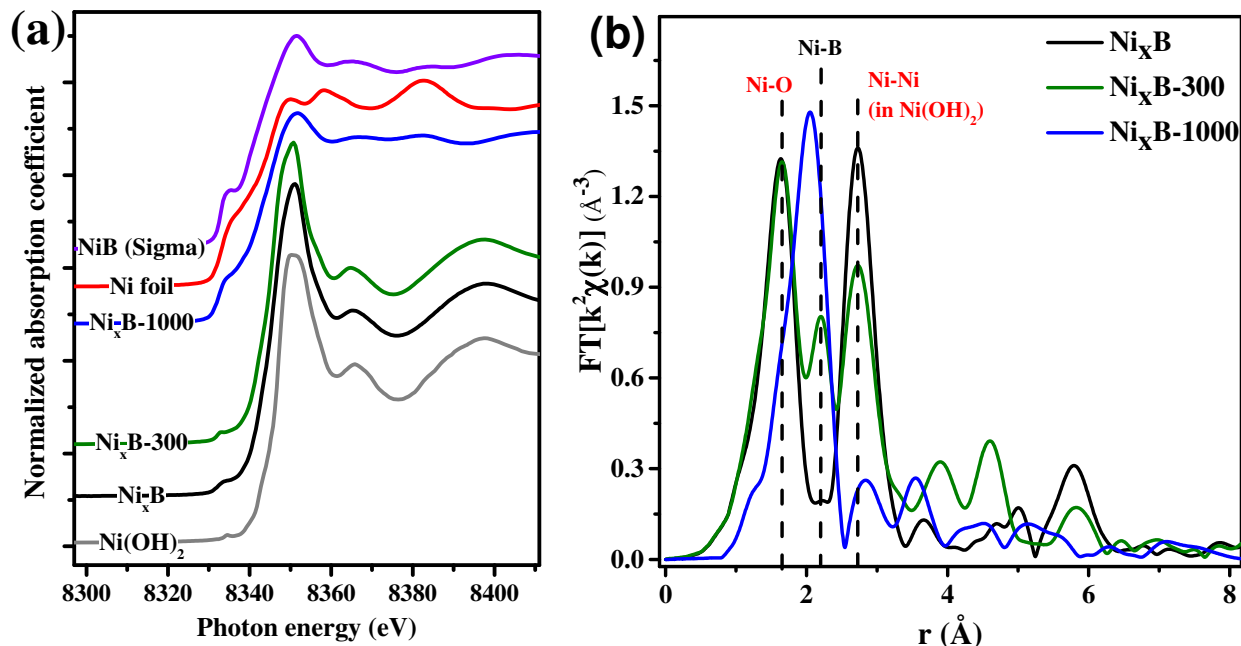

Figure 2| XPS analysis: (a) Ni 2p (a) and (b) B 1s core-level spectra of Ni_xB minimally exposed to air (i) and after prolonged air exposure (ii). (c) Ni 2p core-level spectra of Ni_xB and Ni_xB after

118 annealing under argon at 300 °C, and (d) O 1s high-resolution spectra of Ni_xB-300 before and
119 after electrochemical activation.

120

121
122 **Figure 3 |** (a) X-ray absorption near-edge structure (XANES) spectra of the as prepared Ni_xB
123 sample, Ni_xB annealed at 300 °C (Ni_xB-300) under argon, Ni_xB annealed at 1000 °C under argon
124 (Ni_xB-1000), a Ni-foil, NiB (Sigma Aldrich) and $Ni(OH)_2$ as references. (b) Extended X-ray
125 absorption fine structure (EXAFS) spectra of Ni_xB, Ni_xB-300, and Ni_xB-1000.

126

127   X-ray absorption fine-structure spectroscopy (XAFS) measurements were carried out on

128 Ni_xB, Ni_xB-300 and Ni_xB-1000 to probe the influence of annealing temperature on the chemical

129 state and local coordination structure of the catalyst. X-ray absorption near edge structure

130 (XANES) spectra are presented in Figure 3(a). The pre-edge region of Ni_xB and Ni_xB-300

131 consist of a small peak at ca. 8327.2 eV whose shape and position match very well with $Ni(OH)_2$

132 and NiO (not shown) reference spectra. The first feature above the absorption edge (white-line)

133 centred at 8344.6 eV, is also in agreement with the NiO and $Ni(OH)_2$ spectra, thus indicating

134 predominance of the Ni^{2+} state in the samples. On the other hand, the XANES spectrum of Ni_xB-

135 1000 shows close resemblance to a commercial nickel boride reference (Sigma Aldrich),

136 featured by a white line significantly less intense than the Ni^{2+} references. In this case, the

137 XANES results are in good agreement with XRD data described before. However, the reference

138 nickel boride sample, NiB (Sigma-Aldrich) was composed of several distinct Ni_xB_y phases and

139 was thus not a suitable reference for discussion of the EXAFS data following hereafter.

140 Extended X-ray absorption fine-structure (EXAFS) spectra of Ni_xB, Ni_xB-300 and Ni_xB-

141 1000 (Fig. 3b) reveal significant differences induced by the annealing processes on the local

142 environment of nickel. The shape of both Ni_xB and Ni_xB-300 spectra show the presence of

143 backscattering events characteristic of Ni^{2+} compounds, namely Ni-O at 2.07 Å and Ni-Ni at 3.1

144 Å (uncorrected for phase shift). There is an extra peak emerging at 2.2 Å (uncorrected) on the

145 EXAFS spectrum of the sample annealed at 300°C indicating the presence of B in a local Ni

146 environment. Moreover, peak separation of the spectrum for the untreated Ni_xB sample with a

147 plateau between 2.1 and 2.3 Å gives hint of a similar Ni-B coordination. Detailed analysis of the

148 EXAFS spectra performed by fitting a combination of Ni-O, Ni-B and Ni-Ni^{2+} backscattering

149 paths to the spectral features described above, gives proof to the hypothesis of the presence of

150 boron as nearest neighbour in Ni local coordination (see Table S2 for details). Thus, in the as

151 prepared Ni_xB sample, the effective Ni-B coordination number is as low as 1.8, while a high

152 value of the corresponding σ^2 ($11.9 \cdot 10^{-3}$ Å^2) indicates significant disorder in the boride structure.

153 Annealing at 300 °C results in an increase of the Ni-B coordination number to 4.2, and ordering

154 of the boride structure with a less ordered $Ni(OH)_2$ phase evidenced by a lower Ni-Ni^{2+}

155 coordination number and higher σ^2. The EXAFS spectrum of Ni_xB-1000 is dominated by a peak

156 at 2.05 Å (uncorrected), and can be fitted for the most by Ni-B and a minor amount of Ni-O. The

157 Ni-B coordination number as high as 13.4 in this case can be interpreted by overlapping of

158 several Ni-B backscattering events from different well-ordered Ni_xB_y phases, as indicated by

159 XRD.

160

Electrocatalysis of the oxygen evolution reaction (OER)

162 A film of Ni_xB was adsorbed on a glassy carbon electrode and investigated for

163 electrocatalysis of OER in 0.1 M KOH (see SI for details of film preparation). Before acquiring

164 any electrochemical data, the electrode was first subjected to continuous potential cycling at a

165 scan rate of 0.1 V s^{-1} between 0.95 to 1.65 V (RHE) until reproducible voltammograms were

166 obtained (Fig. 3a). The continuous increase in the intensity of both the anodic and cathodic peaks

167 centred at about 1.40 V is due to growth of a NiOOH layer (Fig. 2d). The anodic process is due

168   to oxidation of Ni^{2+} to Ni^{3+}, while the reverse process is the reduction of Ni^{3+} back to Ni^{2+}, that is,

169    $Ni(OH)_2 + OH^- \leftrightarrow NiOOH + H_2O + e^-$. Results for OER electrocatalysis by Ni_xB in 0.1 M KOH

170   are presented in Fig. 3b. The OER activity of Ni_xB became enhanced upon annealing in argon for

171   2 hours, reaching a maximum at 300 ^{o}C followed by a drastic decline at higher annealing

172   temperatures. The catalyst was not able to attain 10 mA cm^{-2} within the investigated potential

173   window (1.0 - 1.8 V) when annealed at or above 700 ^{o}C. The inset of Fig. 3b shows variation of

174   the OER activity of Ni_xB with annealing temperature, expressed as the potential corresponding to

175   a current density of 10 mA cm^{-2}. The non-annealed sample, Ni_xB, attained 10 mA cm^{-2} at 1.73 V,

176   while Ni_xB-200 and Ni_xB-300 afforded 1.68 and 1.61 V, respectively, at the same current density.

177   Importantly, Ni_xB-300 exhibited better OER activity than Ni_xB-200 despite the former

178   possessing a slightly lower BET surface area, 122.3 m^2 g^{-1} for Ni_xB-300 versus 127.4 m^2 g^{-1} for

179   Ni_xB-200 (Table S1). This implies that increase of the OER activity from Ni_xB through Ni_xB-

180   200 and Ni_xB-300, cannot be explained in terms of surface area.

181   It is worth to note that the intensity of the $Ni^{2+} \leftrightarrow Ni^{3+}$ redox peaks followed a trend

182   exactly similar to the OER activity dependence on temperature. Characteristically, the area under

183   the $Ni^{2+} \leftrightarrow Ni^{3+}$ redox peaks is proportional to the amount of electrochemically addressable

184   nickel atoms/ions, which is intimately linked to conductivity. The observed enhancement of the

185   OER activity with annealing temperature is thus mainly attributed to an increase of the electrical

186   conductivity of the catalyst due to sintering of the catalyst particles. Besides affecting the

187   geometrical properties, XPS analysis revealed that the annealing process also induces changes in

188   the chemical state of the catalyst surface ascribed to electronic structure modification. For

189   example, a positive chemical shift in the BE of the Ni 2p3/2 peak of 0.95 eV, from 852.4 eV to

190   853.5 eV, was observed when Ni_xB was annealed at 300 ^{o}C (Fig. 2c). The decline in activity at

191   much higher annealing temperatures is certainly due to decrease of the surface area due to the

192   growth in particle size. The BET surface area decreased from 122.3 m^2 g^{-1} for Ni_xB-300 to 16.3

193   m^2 g^{-1} for Ni_xB-600, and to 7.9 m^2 g^{-1} for Ni_xB-1000.

194
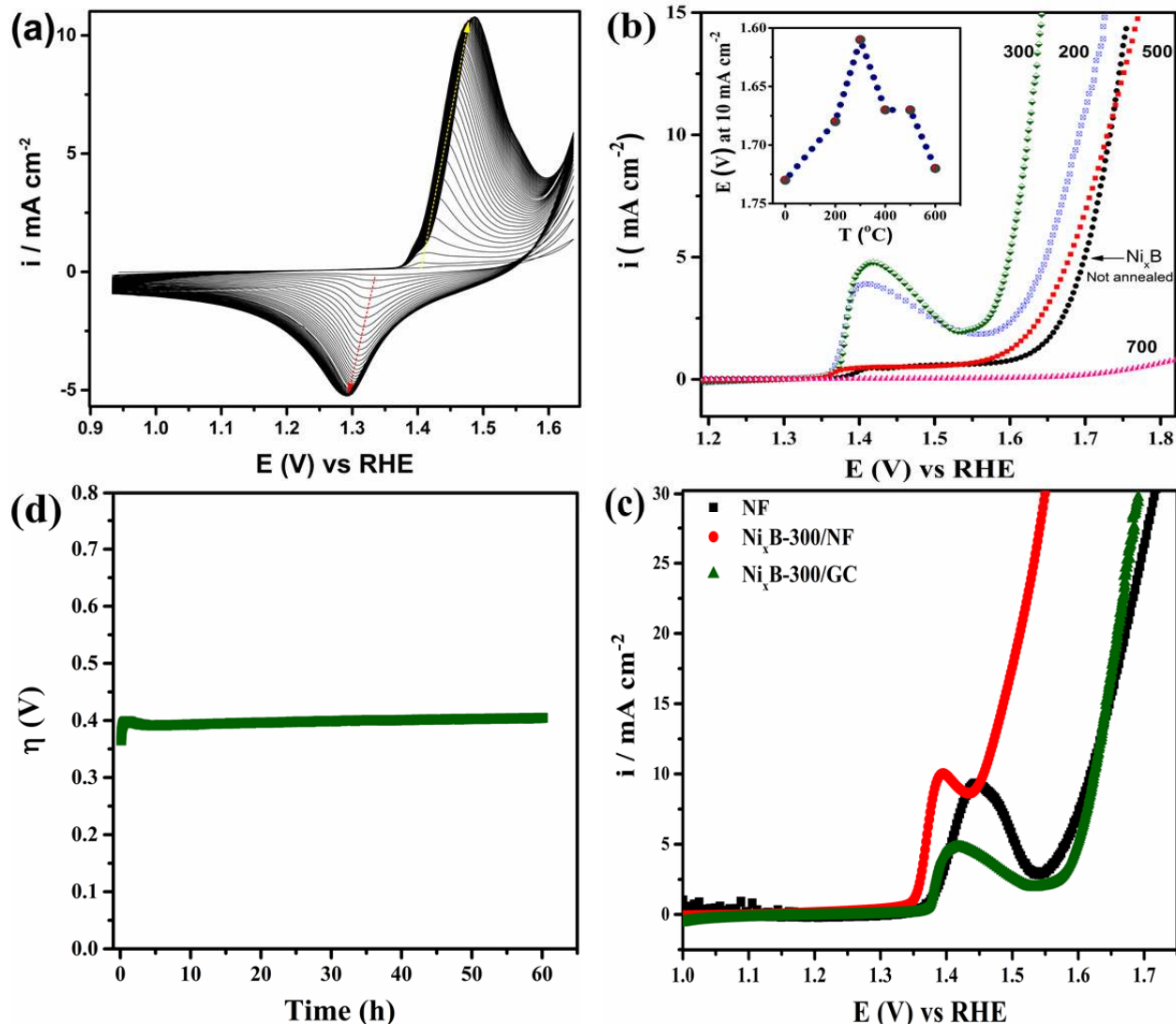
Figure 4 | (a) Activation of Ni$_x$B by continuous potential cycling between 0.95 V and 1.65 V at 100 mV s^{-1} in 0.1 M KOH; (b) Linear sweep voltammograms (LSVs), corrected for the resistance of the electrolyte, of Ni$_x$B and Ni$_x$B annealed at 200 ^{o}C, 300 ^{o}C, 500 ^{o}C and 700 ^{o}C, recorded at 10 mV s^{-1} in 0.1 M KOH and at 1600 rpm electrode rotation. Inset: variation of the OER activity of Ni$_x$B, expressed as the potential at a current density of 10 mA cm^{-2}, with annealing temperature. (c) Galvanostatic long-term stability measurement of Ni$_x$B-300 deposited on a graphite rotating disk electrode (area = 0.196 cm^2) at 10 mA cm^{-2} in KOH (0.1 M); (d) comparative LSVs of a bare nickel foam (NF) electrode, and Ni$_x$B-300 supported on glassy carbon (Ni$_x$B-300/GC) and on nickel foam (Ni$_x$B@NF).

206   Galvanostatic long-term stability measurements of Ni_xB-300 supported on a graphite
207   RDE electrode at a current density of 10 mA cm^{-2} in 0.1 M KOH indicate very stable
208   performance of the catalyst with essentially no loss in performance after 60 h (Fig. 4c). In metal
209   borides, the boron atoms are capable of forming linear, planar and three-dimensional structures
210   surrounded by metals,[9,25] through the formation of covalent M-B, as well as B-B bonds, making
211   these compounds extremely hard and chemically resistant.

212   Nickel foam is an attractive 3D catalyst support for gas evolution electrodes owing to its
213   high surface area, stability and synergistic catalytic effect.[9,26,26–31] We supported Ni_xB-300 on
214   nickel foam (Ni_xB-300/NF) and investigated the resulting electrodes for the OER in a custom-
215   built flow-through cell[32]. Figure 5a shows the OER performance of the Ni_xB-300/NF electrode in
216   0.1 M KOH compared to Ni_xB-300 supported on glassy carbon (Ni_xB-300/GC), and bare NF.
217   Employing NF as a support led to tremendous increase of the current and significant reduction of
218   the overpotential. In our case, it was not valid anymore to extract the potential corresponding to a
219   current density of 10 mA cm^{-2} since this overlapped with the gigantic $Ni^{2+} \rightarrow Ni^{3+} + e^{-}$ oxidation
220   wave. A current density of 20 mA cm^{-2} (normalized to geometric electrode area) was attained at
221   an overpotential of only 0.28 V. To benchmark the performance of Ni_xB-300, its activity was
222   compared against some recently reported highly active non-precious OER catalysts, particularly,
223   nickel based catalysts supported on nickel foam (Table S3). As an example, a NiFe double layer
224   hydroxide doped with nitrogen (N-NiFe-LDH) directly grown on nickel foam, one of the best
225   OER catalysts, afforded 0.23 V overpotential at a current density of 10 mA cm^{-2} in 0.1 M KOH
226   [33]. The performance of Ni_xB-300 is thus clearly very promising and among the best reported for
227   nickel based catalysts.

228

Operando XAFS studies

230   The chemical state and structure of the catalyst under OER conditions was probed via
231   *operando* XAFS studies. Figure 5 presents overlaid *operando* XANES (a) and EXAFS (b)
232   spectra of Ni_xB-300 after electrochemical conditioning between 1.0 V and 1.6 V, during
233   polarization at 1.0 V, a potential below the redox transition from Ni^{2+} ($Ni(OH)_2$) to Ni^{3+}
234   (NiOOH), and at 1.7 V, a potential at which oxygen evolution takes place. The XANES spectra
235   of the pre-conditioned sample and during the polarization at 1.0 V do not show any differences
236   compared to the initial state. Under OER conditions, the Ni-K edge position remains unchanged

237 as well, although there are clear changes in both the slope and specific features of the spectrum.

238 The spectrum measured at 1.7 V has a lower white line intensity with its maximum shifted to

239 higher energy. It resembles the spectrum of NiOOH, produced by *in-situ* electrochemical

240 oxidation of Ni(OH)$_2$ at 1.6 V_{RHE} and is also similar to the spectra of Ni^{3+} species reported in the

241 literature[34,35]. This change observed under reaction conditions indicates that there was a change

242 in the oxidation state from Ni^{2+} to Ni^{3+} (NiOOH) taking place under OER conditions[34,35].

243
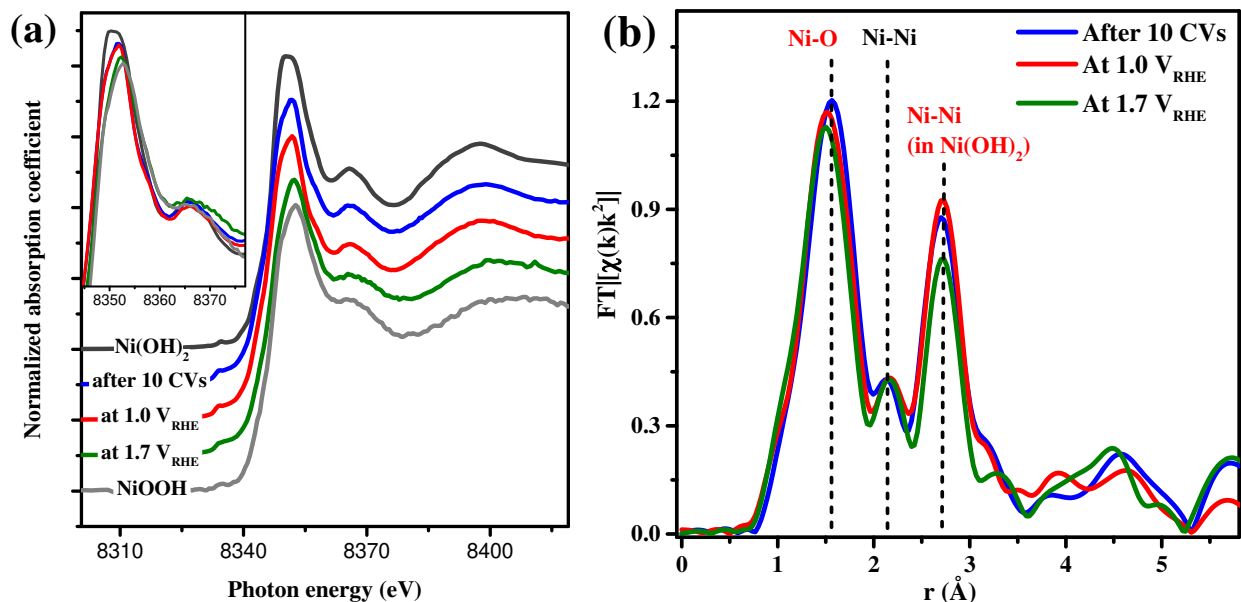
Figure 5 | *Operando* XANES (a) and EXAFS (b) spectra of Ni$_x$B-300 acquired after
conditioning (10 CVs) during OER at different electrochemical potentials, 1.0 V and 1.7 V
versus RHE.

248 The EXAFS spectra measured under *operando* conditions resemble well those of Ni$_x$B-

249 300 measured *ex-situ*, showing the presence of both Ni(OH)$_2$ structure (peaks at 1.55 and 2.73 Å

250 corresponding to Ni-O and Ni-Ni^{2+} backscattering), and Ni-B in the first coordination sphere

251 represented by a small peak at 2.15 Å (all uncorrected for a phase shift). The fitted Ni-O distance

252 does not change after the electrochemical cycling pre-treatment as compared to the untreated

253 sample, but reduces first to 2.05 Å at 1.0 V and then to 2.03 Å at 1.7 V (see Table S4). At the

254 same time, the corresponding coordination numbers decrease from 3.7 to 3.3 and 3.0 for the pre-

255 conditioned sample, and during polarization at 1.0 V and at 1.7 V, respectively. The Ni-Ni^{2+}

256 coordination number changes drastically from 5.7 to 4.0 when comparing the prepared sample to

257 that measured under operando conditions at 1.7 V. The changes observed in the EXAFS features,

258 associated with the Ni^{2+} state can have twofold explanation. Firstly, the significant change of

259 coordination number in the Ni-Ni^{2+} backscattering pair compared to Ni-O points to a less ordered

260 structure under harsh OER conditions since the more distant coordination shells are more

261 sensitive to a material's long range order. Another explanation is associated with the chemical

262 state changes observed on the XANES spectra. Both $Ni(OH)_2$ and $NiOOH$ structures form Ni-O

263 as well as Ni-Ni^{X+} (X = 2, 3) backscattering signals, however shifted by ca. 0.3 Å towards

264 shorter distances in the case of Ni^{3+}. When both structures are present in the sample, the

265 corresponding photoelectron waves interfere destructively due to phase mismatch. This

266 hypothesis is supported by the apparent contraction of the Ni-O bond observed at 1.7 V_{RHE},

267 consistent with observations by other groups[36,37].

268 In the abridged mechanism of O_2 evolution,[38,39] involving the reaction sequence: (i) $M +$

269 $OH^- \rightarrow MOH + e^-$; (ii) $MOH + OH^- \rightarrow MO + H_2O + e^-$; (iii) $MO + OH^- \rightarrow MOOH + e^-$; (iv)

270 $MOOH + OH^- \rightarrow MO_2 + H_2O + e^-$; and (v) $MO_2 \rightarrow M + O_2$, equations (i) to (iii) all involve

271 growth of an oxide layer. In (i) and (ii), Ni is present as Ni^{2+}, while (iii) involves Ni^{2+} to Ni^{3+}

272 transition, and in (iv) Ni^{3+} is oxidized to Ni^{4+}. Based on this mechanism, a fingerprint of Ni^{4+}

273 should be trackable under active oxygen evolution conditions using a suitable *operando*

274 technique[36]. By employing *pseudo-operando* XAFS, and other complementary *in-situ* techniques

275 to track the redox states of Ni and Fe in a Ni-Fe(OOH) catalyst, Strasser et al.[36,40], observed that,

276 for a low content of Fe in the catalyst, < 4%, Ni^{4+} was the dominant redox state of Ni under

277 catalytic OER conditions. Conversely, a high Fe content, > 4%, stabilized the Ni^{2+} state thereby

278 suppressing the higher-valent states of Ni (Ni^{3+} and Ni^{4+}) under catalytic O_2 evolution

279 conditions, resulting in faster oxygen evolution kinetics at the expense of the oxidation of Ni^{2+}.

280 The authors concluded based on these observations, that $Ni^{2+}Fe^{3+}OOH$, is the active state of the

281 Ni-Fe(OOH) catalyst under catalytic conditions. For bulk electrode materials, the OER takes

282 place on a thin surface oxide-hydroxide layer making it challenging to observe the transient

283 states of OER catalysts whose bulk properties predominate the surface properties by employing

284 an averaging technique. The Ni_xB-300 catalyst probed here comprised of ultrathin sheets of

285 atomic scale thickness (≈ 6.6 Å), with a core-shell (Ni-B@NiO_x) structure, where the surface

286 properties (Ni^{2+}) predominated the core properties (Ni-B), as demonstrated by XAFS in Fig. 3,

287 which makes the catalyst suitable for *operando* XAFS studies. Our *operando* XAFS studies did

288 not disclose any features attributable to the Ni^{4+} state at active O_2 evolution potentials. To

rationalize this observation on the premise of the mechanism outlined above, deoxygenation of the NiO_2 intermediate, step (v) has to be comparatively faster in relation to the other reaction steps. Interestingly, our observations lead to a conclusion which appears to be coherent with the work of Strasser et al.[36,40]. Our findings there present new insights into the dynamics of OER catalyst structures under reaction conditions, as well as the dynamics of some transient states of the catalyst during the OER.

Conclusions

Nickel boride (Ni_xB) comprised of very thin sheets and small nanoparticles with a Ni-B core and nickel hydroxide shell (Ni-B@Ni(OH)$_2$) structure is unveiled as a highly efficient and stable electrocatalyst for oxygen evolution under alkaline conditions. When supported on nickel foam, the catalyst drives the OER at 20 mA cm^{-2} at only 0.28 V overpotential in 1.0 M KOH. We observed by operando XAFS, intactness of the Ni-B core under active oxygen evolution, and simultaneously, a transition of Ni^{2+} to Ni^{3+} (NiOOH) in the shell leading to shortening of Ni-O bonds and increase in disorder of the nickel oxyhydroxide layer. The synthesis of nickel boride is simple and readily scalable, making it a very attractive and competitive non-precious anode catalyst in ECWS for mass hydrogen production.

References

1. Barbir, F. PEM electrolysis for production of hydrogen from renewable energy sources. *Solar Energy* **78,** 661–669 (2005).

2. Zeng, K. & Zhang, D. Recent progress in alkaline water electrolysis for hydrogen production and applications. *Prog. Energ. Combust* **36,** 307–326 (2010).

3. Reier, T., Oezaslan, M. & Strasser, P. Electrocatalytic Oxygen Evolution Reaction (OER) on Ru, Ir, and Pt Catalysts: A Comparative Study of Nanoparticles and Bulk Materials. *ACS Catal.* **2,** 1765–1772 (2012).

4. Lee, Y., Suntivich, J., May, K. J., Perry, E. E. & Shao-Horn, Y. Synthesis and Activities of Rutile IrO 2 and RuO 2 Nanoparticles for Oxygen Evolution in Acid and Alkaline Solutions. *J. Phys. Chem. Lett,* 399–404 (2012).

5. Han, L., Dong, S. & Wang, E. Transition-Metal (Co, Ni, and Fe)-Based Electrocatalysts for the Water Oxidation Reaction. *Adv. Mater.* **28,** 9266–9291 (2016).

320   6. Anantharaj, S. *et al.* Recent Trends and Perspectives in Electrochemical Water Splitting with
321   an Emphasis on Sulfide, Selenide, and Phosphide Catalysts of Fe, Co, and Ni. A Review.
322   *ACS Catal.* **6,** 8069–8097 (2016).

323   7. Enman, L. J., Burke, M. S., Batchellor, A. S. & Boettcher, S. W. Effects of Intentionally
324   Incorporated Metal Cations on the Oxygen Evolution Electrocatalytic Activity of Nickel
325   (Oxy)hydroxide in Alkaline Media. *ACS Catal.* **6,** 2416–2423 (2016).

326   8. Burke, M. S., Kast, M. G., Trotochaud, L., Smith, A. M. & Boettcher, S. W. Cobalt-iron
327   (oxy)hydroxide oxygen evolution electrocatalysts: the role of structure and composition on
328   activity, stability, and mechanism. *J. Am. Chem. Soc.* **137,** 3638–3648 (2015).

329   9. Lu, X. & Zhao, C. Electrodeposition of hierarchically structured three-dimensional nickel-
330   iron electrodes for efficient oxygen evolution at high current densities. *Nat Comms* **6,** 6616
331   (2015).

332   10. Gong, M. *et al.* An advanced Ni-Fe layered double hydroxide electrocatalyst for water
333   oxidation. *J. Am. Chem. Soc.* **135,** 8452–8455 (2013).

334   11. Song, F. & Hu, X. Exfoliation of layered double hydroxides for enhanced oxygen evolution
335   catalysis. *Nat Comms* **5,** 4477 (2014).

336   12. Masa, J. *et al.* Low Overpotential Water Splitting Using Cobalt–Cobalt Phosphide
337   Nanoparticles Supported on Nickel Foam. *ACS Energy Lett.* **1,** 1192–1198 (2016).

338   13. Popczun, E. J. *et al.* Nanostructured Nickel Phosphide as an Electrocatalyst for the Hydrogen
339   Evolution Reaction. *J. Am. Chem. Soc.* **135,** 9267–9270 (2013).

340   14. Popczun, E. J., Read, C. G., Roske, C. W., Lewis, N. S. & Schaak, R. E. Highly Active
341   Electrocatalysis of the Hydrogen Evolution Reaction by Cobalt Phosphide Nanoparticles.
342   *Angew. Chem. Int. Ed.* **53,** 5427–5430 (2014).

343   15. Long, X. *et al.* Metallic Iron-Nickel Sulfide Ultrathin Nanosheets As a Highly Active
344   Electrocatalyst for Hydrogen Evolution Reaction in Acidic Media. *J. Am. Chem. Soc.* **137,**
345   11900–11903 (2015).

346   16. Zhu, W. *et al.* Nickel sulfide microsphere film on Ni foam as an efficient bifunctional
347   electrocatalyst for overall water splitting. *Chem. Commun* **52,** 1486–1489 (2016).

348   17. Zhou, H. *et al.* Efficient hydrogen evolution by ternary molybdenum sulfoselenide particles
349   on self-standing porous nickel diselenide foam. *Nat Comms* **7,** 12765 (2016).

350   18. Vrubel, H. & Hu, X. Molybdenum Boride and Carbide Catalyze Hydrogen Evolution in both
351   Acidic and Basic Solutions. *Angew. Chem. Int. Ed.* **124,** 12875–12878 (2012).

352   19. Glavee, G. N., Klabunde, K. J., Sorensen, C. M. & Hadjapanayis, G. C. Borohydride
353   reductions of metal ions. A new understanding of the chemistry leading to nanoscale particles
354   of metals, borides, and metal borates. *Langmuir* **8,** 771–773 (1992).

355   20. Blanchard, P. E. R., Grosvenor, A. P., Cavell, R. G. & Mar, A. X-ray Photoelectron and
356   Absorption Spectroscopy of Metal-Rich Phosphides M_2P and M_3P (M = Cr−Ni). *Chem.*
357   *Mater.* **20,** 7081–7088 (2008).

358   21. Schreifels, J. X-Ray photoelectron spectroscopy of nickel boride catalysts: Correlation of
359   surface states with reaction products in the hydrogenation of acrylonitrile. *J. Catal.* **65,** 195–
360   206 (1980).

361   22. Carenco, S., Portehault, D., Boissière, C., Mézailles, N. & Sanchez, C. Nanoscaled metal
362   borides and phosphides: recent developments and perspectives. *Chem. Rev.* **113,** 7981–8065
363   (2013).

364   23. Demirci, U. B. & Miele, P. Cobalt in NaBH4 hydrolysis. *Phys. Chem. Chem. Phys.* **12,**
365   14651–14665 (2010).

366   24. Arzac, G. M., Rojas, T. C. & Fernández, A. New insights into the synergistic effect in
367   bimetallic-boron catalysts for hydrogen generation: The Co–Ru–B system as a case study.
368   *Appl. Catal., B* **128,** 39–47 (2012).

369   25. Shveikin, G. P. & Ivanovskii, A. L. The chemical bonding and electronic properties of metal
370   borides. *Russ. Chem. Rev.* **63,** 711–734 (1994).

371   26. Tang, C., Cheng, N., Pu, Z., Xing, W. & Sun, X. NiSe Nanowire Film Supported on Nickel
372   Foam: An Efficient and Stable 3D Bifunctional Electrode for Full Water Splitting. *Angew.*
373   *Chem. Int. Ed.* **54,** 9351–9355 (2015).

374   27. Ledendecker, M. *et al.* The Synthesis of Nanostructured Ni5 P4 Films and their Use as a
375   Non-Noble Bifunctional Electrocatalyst for Full Water Splitting. *Angew. Chem. Int. Ed.*
376   (2015).

377   28. Stern, L.-A., Feng, L., Song, F. & Hu, X. Ni 2 P as a Janus catalyst for water splitting. The
378   oxygen evolution activity of Ni_2P nanoparticles. *Energy Environ. Sci.* **8,** 2347–2351 (2015).

379   29. Shalom, M. *et al.* Nickel nitride as an efficient electrocatalyst for water splitting. *J. Mater.*
380   *Chem. A* **3,** 8171–8177 (2015).

381   30. Zhu, Y.-P., Liu, Y.-P., Ren, T.-Z. & Yuan, Z.-Y. Self-Supported Cobalt Phosphide
382   Mesoporous Nanorod Arrays. A Flexible and Bifunctional Electrode for Highly Active
383   Electrocatalytic Water Reduction and Oxidation. *Adv. Funct. Mater,* **25** 7337–7347 (2015).

384   31. Zhou, W. *et al.* Ni_3S_2 nanorods/Ni foam composite electrode with low overpotential for
385   electrocatalytic oxygen evolution. *Energy Environ. Sci.* **6,** 2921–2924 (2013).

386   32. Maljusch, A., Conradi, O., Hoch, S., Blug, M. & Schuhmann, W. Advanced Evaluation of the
387   Long-Term Stability of Oxygen Evolution Electrocatalysts. *Anal. Chem* **88,** 7597–7602
388   (2016).

389   33. Chen, S. *et al.* Three-Dimensional Smart Catalyst Electrode for Oxygen Evolution Reaction.
390   *Adv. Energy Mater.* **5,** 1500936 (2015).

391   34. Gul, S. *et al.* Simultaneous detection of electronic structure changes from two elements of a
392   bifunctional catalyst using wavelength-dispersive X-ray emission spectroscopy and in situ
393   electrochemistry. *Phys. Chem. Chem. Phys.* **17,** 8901–8912 (2015).

394   35. Mansour, A. N. X-Ray Absorption Fine Structure Spectra and the Oxidation State of Nickel
395   in Some of Its Oxycompounds. *J. Electrochem. Soc.* **141,** L69-L71 (1994).

396   36. Gorlin, M. *et al.* Oxygen Evolution Reaction Dynamics, Faradaic Charge Efficiency, and the
397   Active Metal Redox States of Ni-Fe Oxide Water Splitting Electrocatalysts. *J. Am. Chem.*
398   *Soc.* **138,** 5603–5614 (2016).

399   37. Dionigi, F. & Strasser, P. NiFe-Based (Oxy)hydroxide Catalysts for Oxygen Evolution
400   Reaction in Non-Acidic Electrolytes. *Adv. Energy Mater.* **6,** 1600621 (2016).

401   38. Matsumoto, Y. & Sato, E. Electrocatalytic properties of transition metal oxides for oxygen
402   evolution reaction. *Mater. Chem. Phys.* **14,** 397–426 (1986).

403   39. Dau, H. *et al.* The Mechanism of Water Oxidation. From Electrolysis via Homogeneous to
404   Biological Catalysis. *ChemCatChem* **2,** 724–761 (2010).

405   40. Goerlin, M. *et al.* Tracking catalyst redox states and reaction dynamics in Ni-Fe
406   oxyhydroxide oxygen evolution reaction (OER) electrocatalysts: The role of catalyst support
407   and electrolyte pH. *J. Am. Chem. Soc.* (2017). DOI: 10.1021/jacs.6b12250

408

Author Contribution

JM and WS conceived the idea, planned the experiments and wrote the manuscript, IS, HM and BRC performed XAFS measurements, designed cells for operando XAS measurements, discussed and interpreted XAFS data and participated in writing parts of the manuscript, EV contributed in electrochemical experiments, discussion and data interpretation, MdlM, and JA did the (S)TEM and EELS measurements and helped with interpretation of crystallographic data, IS and MM contributed with the XPS measurements, discussions and data interpretation.

Author Information

Correspondence and requests for materials should be addressed to justus.masa@rub.de and wolfgang.schuhmann@rub.de
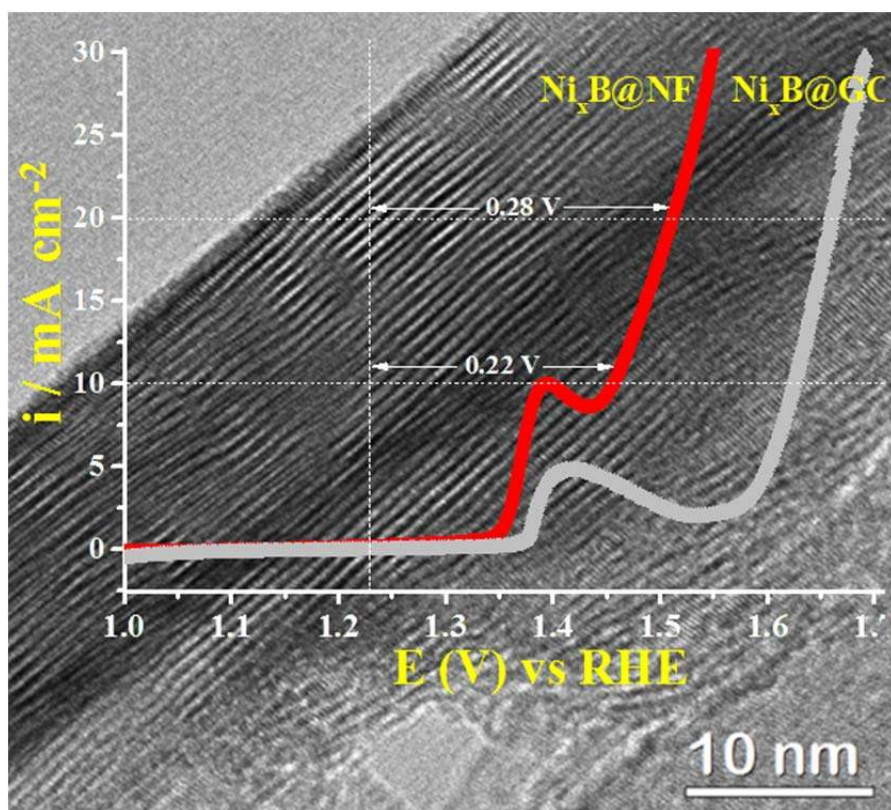
Additional information

Supplementary information, reprints and permissions information is available online at www.nature.com/reprints. Correspondence and requests for materials should be addressed to J.M. and W.S.

438 **Competing financial interests**

439 The authors declare no competing financial interests.

440

441 **Table of contents (TOC) image**

442

443